The final publication is available at

https://doi.org/10.1109/TAP.2023.3253209

Additional Information

Communication

Wideband Circularly-Polarized Mm-Wave Array Antenna Using H-shaped Low-Axial-Ratio Apertures

Jose I. Herranz-Herruzo, *Member, IEEE*, Miguel Ferrando-Rocher, *Member, IEEE*, Alejandro Valero-Nogueira, *Senior Member, IEEE*, and Bernardo Bernardo-Clemente

Abstract—An H-shaped all-metal radiating element comprising an active and a coupled slot has been proposed to design wideband high-efficiency circularly-polarized antenna arrays. The proper excitation of several modes on the coupled slot enables a wide axial ratio bandwidth with high circular polarization purity. In order to feed an array of such radiating elements, a simple and scalable two-layer corporate network, implemented in groove gap waveguide technology, is conceived. Those good frequency properties have been confirmed by the fabrication of a prototype, whose experimental results report a 1-dB axial ratio bandwidth of 22%. In addition, a peak radiation efficiency of 97% with good pattern stability, and an impedance bandwidth of 21% with high return loss, have been measured. The proposed array demonstrates similar bandwidth figures attained by arrays fed by sequential rotation networks but with a much simpler feeding structure and lower axial ratio values, which makes it particularly suitable for Ka-band satellite communications antennas.

Index Terms—antenna arrays, circular polarization, slotted waveguide arrays, satellite communications, gap waveguide.

I. Introduction

Modern mm-wave communication systems call for low-profile high-gain antennas capable of dealing with severe propagation losses in point-to-point links. Circular polarization (CP) is also often required by some of these systems because of its known advantages in terms of eventual polarization mismatch. From the antenna point of view, the high CP purity demanded in Ka-band satellite communications, where ground coverage is provided by adjacent LHCP/RHCP cells, is particularly challenging. In this system, the classical 3-dB axial ratio (AR) threshold is not valid in practice to meet specifications. Instead, an exigent AR value below 1 or 1.5 dB over a wide frequency band is usually requested.

The use of printed technologies to achieve wideband mm-wave CP arrays has been extensively reported in the last decade [1]–[3]. Their well-known advantages in terms of thickness, weight, and cost make them very appealing for low-power applications. However, in addition to their lower power handling capability and mechanical robustness, these solutions exhibit a moderate dielectric loss in mm-wave band.

All-metal arrays fed by hollow waveguides overcome all those drawbacks in exchange for higher weight and fabrication cost, and a slightly increased profile. However, the conception of broadband all-metal CP radiating elements, capable of forming closely-spaced arrays, is not trivial. An intermediate approach involves adding a polarization converter over a conventional slot array. Several dipoles printed on a dielectric superstrate [4], [5] or chamfered metallic apertures [6], [7] can effectively radiate a CP wave over a wide bandwidth, up to 10-15%, with an AR below 3 dB. Noteworthy in this context is the single-layer integration of the chamfered apertures and the feed network, achieved in [8], albeit with a narrower bandwidth.
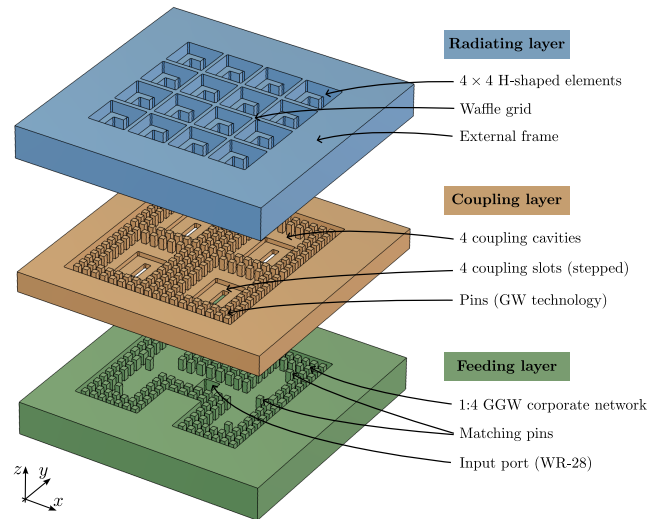
Fig. 1. Exploded view of the array architecture.

As widely known, sequential rotation (SR) feeding schemes provide large AR bandwidths, even with relatively narrowband radiating elements. Despite this fact, implementing such a technique with all-metal waveguides is not trivial, resulting in intricate feeding networks. Among the scarce examples found in literature, it is worth mentioning the recent works [9], [10], achieving AR bandwidths of 22% below 3 dB and 12% below 1.5 dB, respectively.

Some other works, instead, propose wideband CP radiating elements able to be fed by conventional waveguide networks. In a recent work [11], a novel low-profile septum element is used to design an 8×8 array achieving a remarkable 3-dB AR bandwidth of 33%. The antenna element consists of an open widened waveguide and two symmetric stepped septum blades, rather than a septum polarizer, and a pair of side ridges. The size of such an element, however, is too large along one dimension, around $1.3\lambda_0$ at the center frequency, which leads to grating lobes in the upper band.

In this context, a more compact T-shaped CP radiating element was recently proposed [12], formed by an active slot fed by a conventional waveguide, which is coupled to an orthogonal backshorted slot. Despite its feeding simplicity, fabrication ease, and low profile and size, the achieved AR bandwidth remains around 6% and 3% for the 2 dB and 1 dB thresholds, respectively. In this paper, the T-shaped element is modified by tailoring the coupled slot shape to enlarge its AR bandwidth up to 24% below 1 dB. This figure is similar to that reported for sequential rotation networks [9], but here with a much simpler feeding mechanism and lower axial ratio values. Moreover, the radiating element keeps a compact size, around $0.7\lambda_0$, along both dimensions, making it suitable to design mm-wave arrays compatible with typical specifications of Ka-band satellite communications.
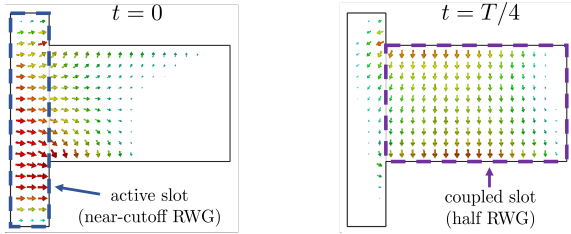
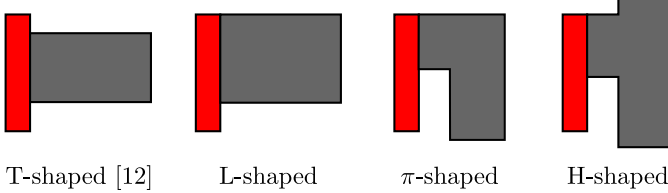Fig. 2. Instantaneous aperture electric field for an LHCP T-shaped element.

Fig. 3. Design evolution (from left to right) of the H-shaped radiating element.

A very brief definition of the proposed radiating element was first outlined in [13], with some preliminary simulation results of a single element. The present work includes a detailed description of the element's operating principle (Section II), the design of a complete 4×4 array (Section III), shown in Fig. 1, and the experimental validation of a fabricated prototype (Section IV). Results discussion and main conclusions of this work are addressed in Section V.

II. RADIATING ELEMENT

The proposed radiating element is derived from the former T-aperture, whose details can be found in [12], and are omitted here for brevity. Basically, this compound element comprises an active and a coupled slot, perpendicular to each other, forming an asymmetrical T-shape. The active slot, conventionally fed by a waveguide, excites the coupled backshorted slot. For illustration, Fig. 2 represents the instantaneous electric field on a sample LHCP T-shaped element. The combined radiation of the electric fields on both slots produces a pure CP wave in the broadside direction.

To meet resonance condition, the length of the active slot is around half free-space wavelength, so it behaves as a near-cutoff rectangular waveguide (RWG). On the coupled slot, conversely, the field resembles that of a half-mode RWG, whose strength is driven by the vertical shift between both slots. Consequently, the coupled slot length governs the propagation constant through the equivalent half RWG and, hence, the phase difference between both aperture field components. As thoroughly explained in [12], these two parameters, length and shift of the coupled slot, can be tuned for an optimum 0-dB AR value at the design frequency.

Following this basic concept, the coupled slot shape can be modified to achieve a wider polarization bandwidth. Four element shapes have been addressed in Fig. 3 to understand the design evolution from the former T-shaped element. The first variant considered moves the coupled slot to the edge of the active slot, forming an L-shaped element. This configuration yields the widest coupled slot possible, which maximizes the AR bandwidth [12]. The next evolution step bends the coupled slot so that the resulting element resembles a letter π shape. In the final step, the right arm of the π shape is shifted vertically, resulting in a kind of asymmetric H-shaped element.

The frequency performance of these new element shapes is analyzed in Figs. 4 and 5. All element dimensions have been optimized to maximize the AR bandwidth, but are omitted here for brevity. Fig. 4 reveals that the T-shaped element achieves a 1-dB AR bandwidth of
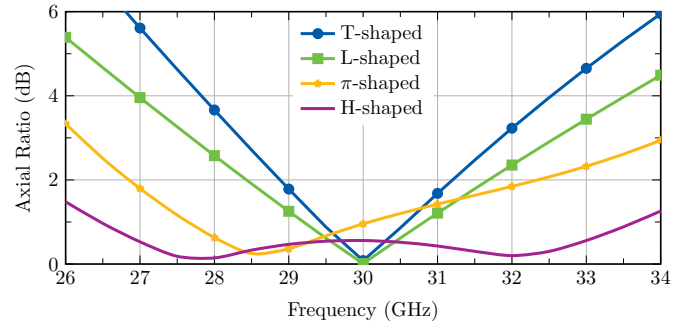

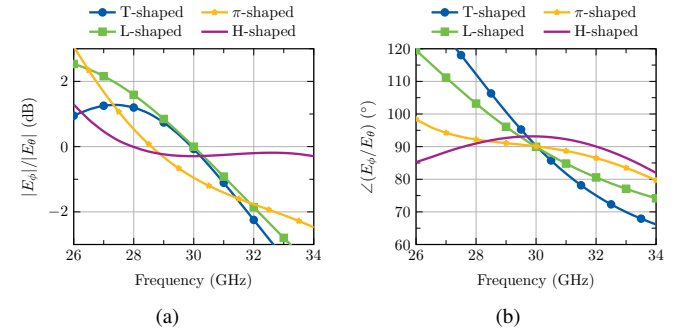Fig. 4. Boresight axial ratio versus frequency for the four element shapes.

(a)

(b)

Fig. 5. Ratio of the boresight radiated field components, in (a) magnitude and (b) phase, for the four element shapes.

3.8%. This value is improved by the L-shaped one to 5.4%. Although the latter figure supposes an appreciable enhancement, both cases rely on the same coupling mechanism leading to a relatively narrowband performance. The main factor behind this behavior is the monomode character of the coupled slot. As shown in Fig. 5(b), for both T- and L-shaped cases, the phase difference between radiated components exhibits a steep linear variation, which is given by the propagation constant of the fundamental mode in the coupled slot.

In light of the above, coupled slots supporting more than one mode may lead to a more uniform phase difference between radiated components. That is the case of the π-shaped element in Fig. 3, in which the fundamental mode excites mainly the vertical electric field component on top of the created ridge, while higher-order modes are related to the horizontal component on the bent arm. As shown in Fig. 5(b), the phase difference for this new element displays much more stability with frequency, because of the inflection points associated to the excitation of several modes. In contrast, the magnitude ratio of the radiated components plotted in Fig. 5(a), exhibits a roughly similar steep variation for T-, L- and π-shaped elements, far from the ideal 0-dB value at band edges. Consequently, the AR response of the π-shaped element in Fig. 4, despite being more wideband than that of the T and L elements, may be subject to further improvement.

In this regard, an additional degree of freedom can be added to the π shape by shifting the vertical arm of the coupled slot vertically. This last evolution step is denoted as the H-shaped element in Fig. 3. By applying this slight movement, the excitation of the higher-order modes can be effectively controlled, and a more stable component ratio can be achieved in either magnitude or phase, as shown in Fig. 5. As a result, an optimized H-shaped element can attain a remarkably wideband AR response in Fig. 4, with a 1-dB AR bandwidth of 23.9%. This value means an improvement ratio above 1:6 concerning the previous T-shaped element.
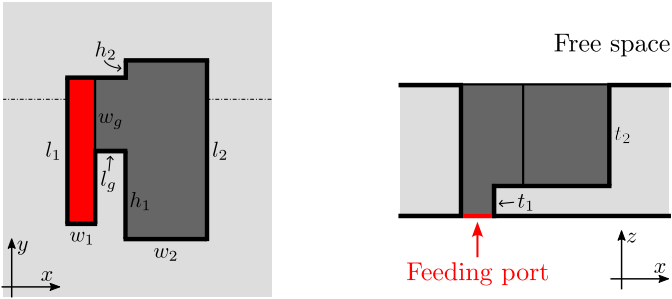
Fig. 6. Geometry of the H-shaped element with all involved dimensions: (a) top view and (b) cross-section side view.

TABLE I
DIMENSIONS (MM) OF AN LHCP H-SHAPED ELEMENT

l_1	w_1	l_g	w_g	l_2	w_2	h_2	t_1	t_2
5.5	1.0	1.0	2.56	7.36	3.70	1.17	1.0	3.5
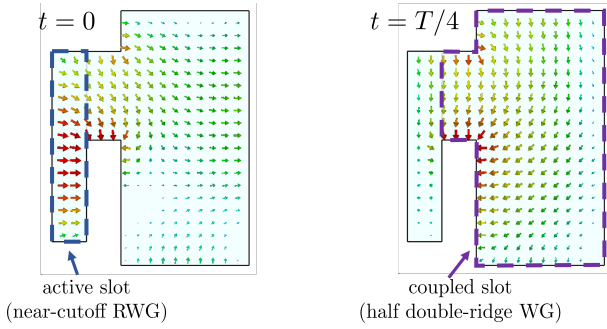
Fig. 7. Instantaneous electric field for an LHCP H-element at 30 GHz.
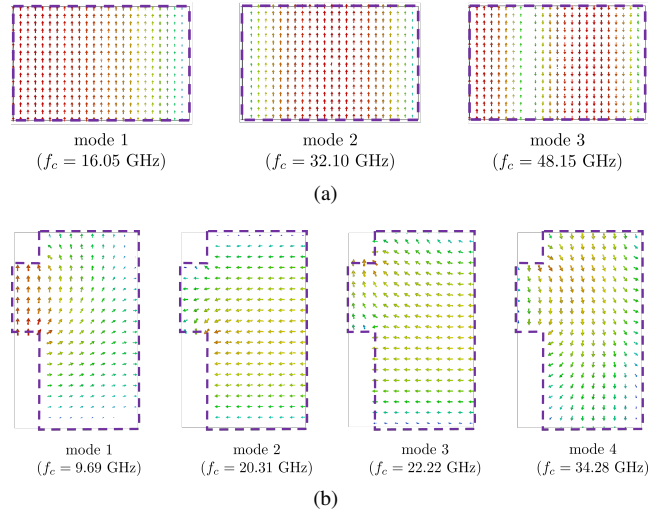

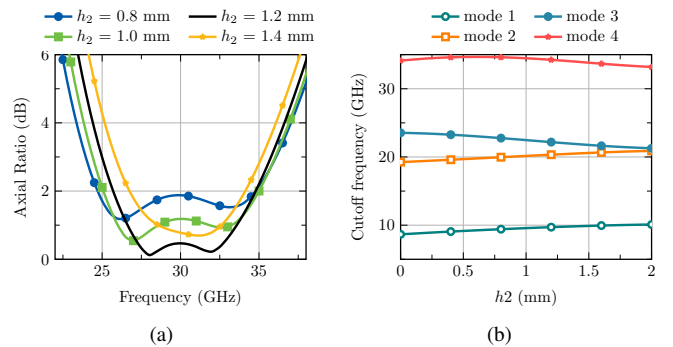Fig. 8. Modes on the coupled slot and their cutoff frequencies for the (a) T- and (b) H-shaped elements.

Fig. 9. (a) Axial ratio versus frequency and (b) cutoff frequencies in the coupled slot, for different h_2 values of the H-element.

The new H-element has been adopted in this work to construct a wideband mm-wave array, and its main operating principle is studied first. Detailed top and side views of this element are depicted in Fig. 6, with all its relevant dimensions. The optimized parameters of the wideband H-element used in Fig. 4 are indicated in Table I. The instantaneous aperture electric field at 30 GHz, which radiates an LHCP wave, is represented in Fig. 7. This graph reveals that the E_y-component (vertical) is mostly excited around the H-shape ridge, while E_x-component (horizontal) is distributed between the active slot and the vertical arm of the coupled slot. In this context, following the above analogy, the active slot of the H-element behaves as a near-cutoff RWG, and the coupled slot is now roughly equivalent to a half double-ridge waveguide (DRWG).

Thereby, the multimode nature of the new H-element can be analyzed by studying the modes supported by such equivalent DRWG. First, the modes corresponding to the T-element (half RWG) are shown in Fig. 8(a), along with their cutoff frequencies. This figure confirms that only the first mode is excited within the 3-dB AR bandwidth (28.3-31.8 GHz). This fact contrasts with the equivalent DRWG of the H-element depicted in Fig. 8(b), which supports three modes within the operating band. As expected, the fundamental mode mostly excites the E_y-component on top of the waveguide ridge, whereas the E_x-component appears dominant for the second and third modes. Note that it is not possible to compute the complex mode excitation of these modes for the compound radiating element since, for simplicity, the eigenmode analysis is only performed on the equivalent half waveguides. A complete study would entail a more complex physical interpretation due to a larger number of modes.

The optimum H-shape dimensions can be easily tuned by conventional optimization techniques. For illustration, Fig. 9(a) plots the AR response for different lengths h_2 of the upper ridge. It can be seen how higher h_2 values bring the two AR minima closer and, hence, this dimension can be tuned to meet specifications in terms of bandwidth or maximum AR threshold. Such behavior versus h_2 parameter derives from the multimode character of the coupled slot. Fig. 9(b) represents the cutoff frequencies of the first modes within the equivalent DRWG. It can be observed how the propagating modes approach each other in frequency for higher h_2 values, a fact consistent with the AR curve in Fig. 9(a). Despite its multimode nature, it is very relevant to emphasize that the proposed H-shaped size is around $0.6\lambda_0 \times 0.7\lambda_0$, which remains compact enough to design arrays without grating lobes.

III. ARRAY DESIGN

To validate the performance of the proposed radiating element, a 4×4 array has been designed and tested experimentally. The array design process is simplified by following a two-step procedure. Firstly, the radiating layer is optimized by simultaneously feeding the 16 H-elements through individual waveguide ports on the back side of the active slots. As shown in Fig. 10, the radiating elements are housed within square cavities to reduce mutual coupling, being the array spacing along both planes $p_x = p_y = 9$ mm. In this case, the optimization process seeks a minimum AR over the targeted bandwidth, from 27 to 33 GHz. The tuned dimensions are summarized in
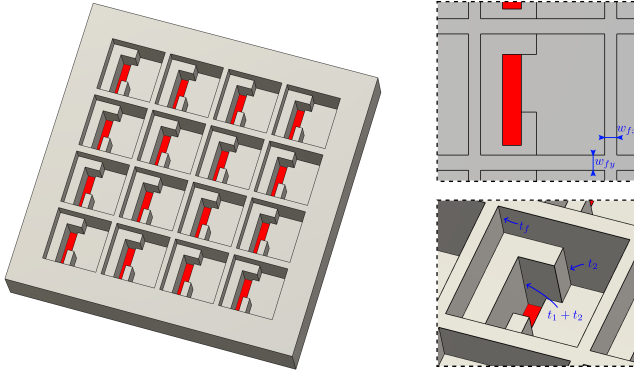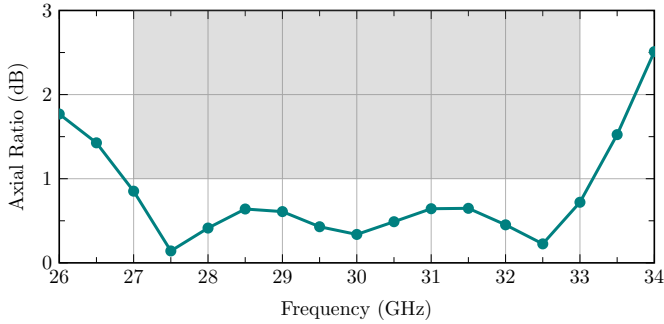
Fig. 10. Radiating layer and zoomed views.

Fig. 11. Axial ratio versus frequency of the radiating layer.
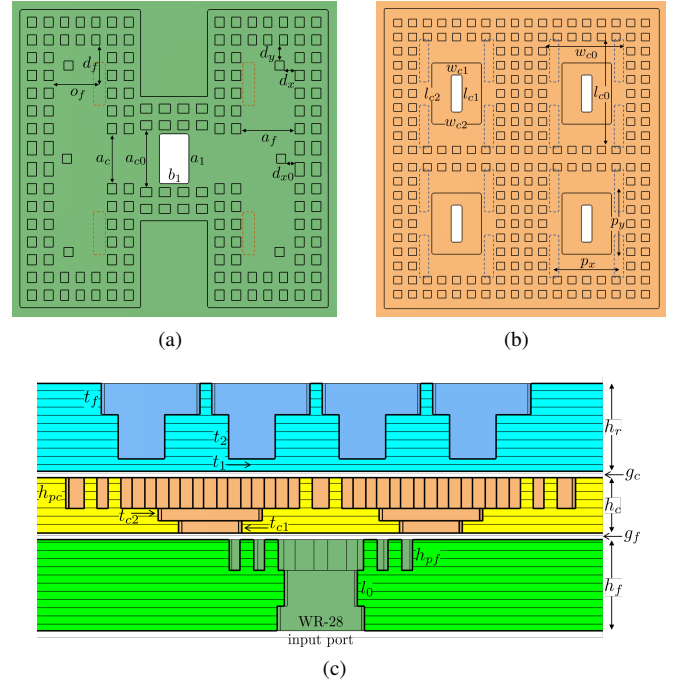

Fig. 12. Top view of (a) the feeding layer (upper coupling slots in dashed line), and (b) the coupling layer (upper radiating slots in dashed line); (c) Cross-section side view of the whole array.

Table II, and the optimized AR curve is plotted in Fig. 11. This result confirms that a wide AR bandwidth is attained. Around 6.3 GHz below 1 dB, although, as expected, slightly narrower than that of the single element case.

Once the radiating elements have been optimized, a corporate-feed network is designed to leverage the wideband array performance. Specifically, a widely used two-layer network architecture [14], based on intermediate coupling cavities, has been adopted here. Such a network is implemented here in groove-gap waveguide (GGW) technology [15], with the aim of avoiding the field leakage between pieces and facilitating the array assembly. To relax CNC fabrication tolerances, a relatively thick gap of 0.4 mm is chosen, with a pin periodicity of 2 mm, and a minimum space of 0.9 mm between pins.

Fig. 1 illustrates the complete array architecture, constituted, from top to bottom, of the radiating, coupling, and feeding layers. More detailed top views of the coupling and feeding layers, and a side view of the entire structure, are depicted in Fig. 12, along with the most relevant dimensions detailed in Table II. Below the radiating layer, the coupling layer comprises 4 rectangular cavities, each feeding 4 H-shaped radiators. In turn, each coupling cavity is fed by a single slot surrounded by a rectangular step, which replaces the usual cavity ridges and simplifies the pin layout, when compared to previous works. Lastly, the bottom layer feeds the coupling slots through a 1:4 GGW corporate network. Simple matching pins are optimally located at each 1:2 splitter, and next to the coupling slots, to achieve a wideband uniform power distribution from the input WR-28 port. Note that this feeding layer adopts a simple and scalable architecture, getting rid of the fine details present in the classical chandelier-like ridge gap waveguide (RGW) approach [16].

The two-layer network described above uniformly feeds the 16 radiating elements. For the sake of illustration, Fig. 13 represents the magnitude of the simulated electric field in the three layers, at

a representative height. This graph reveals the effective role of the matching pins in the feeding layer, the high symmetry of the cavity modes in the coupling layer, and the good illumination uniformity of the radiating elements. In this regard, it can be concluded that the use of sufficiently narrow slots connecting successive layers plays a key role in field uniformity. The rest of the simulated antenna parameters, along with measurements, will be shown in the next section.

IV. EXPERIMENTAL VALIDATION

The designed array is fabricated in aluminum by conventional CNC milling techniques. Four screws and four aligning pins have been located at the array corners to assemble the three aluminum pieces shown in Fig. 14. These pictures give a clear view of the relatively thick gap between pieces. As discussed above, the array architecture has been conceived to relax CNC fabrication tolerances as far as possible.

TABLE II
DIMENSIONS (MM) OF THE 16X16 ARRAY

Radiating layer										
l_1	w_1	l_g	w_g	l_2	w_2	h_2	t_1	t_2	t_0	$w_{0x/y}$
6.0	1.25	1.0	3.79	8.0	4.53	1.35	1.0	3.5	2.5	0.8/1.0

Coupling layer									
l_{c1}	w_{c1}	l_{c2}	w_{c2}	l_{c0}	w_{c0}	t_{c1}	t_{c2}	h_{pc}	g_c
5.12	1.5	8.46	6.85	14.55	11.06	1.0	1.0	2.5	0.4

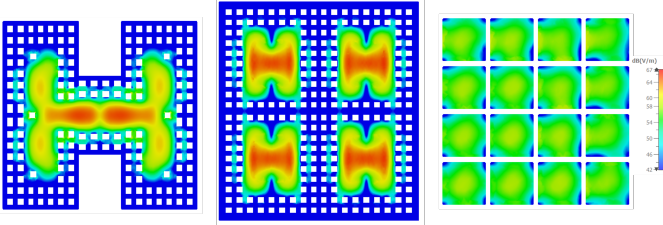| **Feeding layer**									
o_f	d_f	d_x	d_y	d_{x0}	a_f	a_c	a_{c0}	a_1	b_1
5.57	4.67	1.31	1.91	1.12	6.55	5.99	6.96	5.98	3.56
		h_{pf}	g_f	l_0	h_f				
		2.5	0.4	2.91	7.41				

Fig. 13. Magnitude of the electric field at 30 GHz in the feeding (left), coupling (center), and radiating layer (right) of the array.
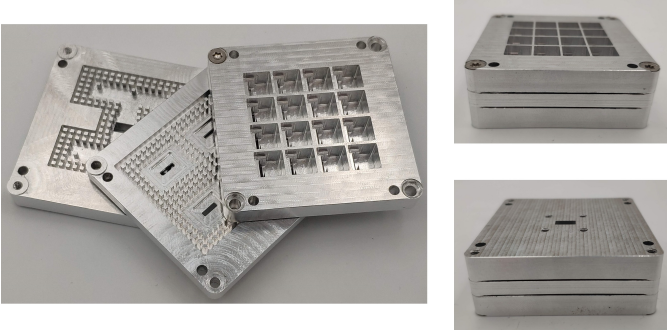

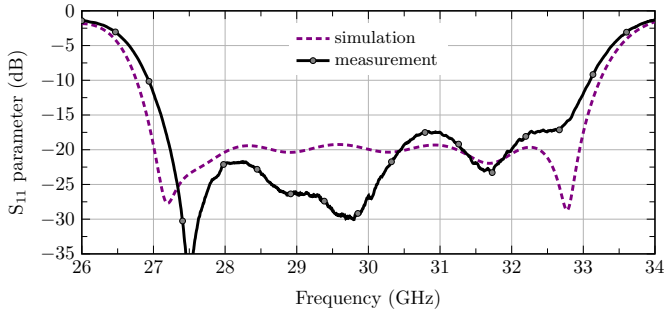Fig. 14. Fabricated prototype: disassembled (right) and assembled (left) array.

Fig. 15. Measured and simulated reflection coefficient versus frequency.
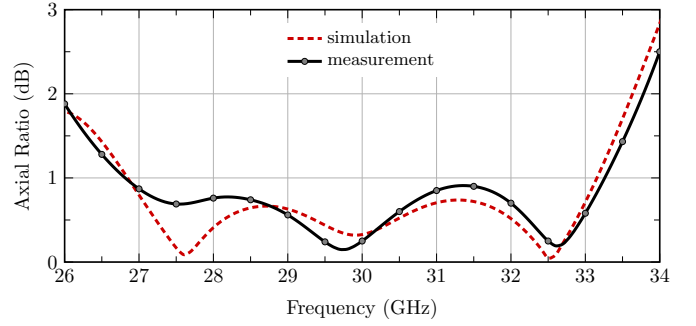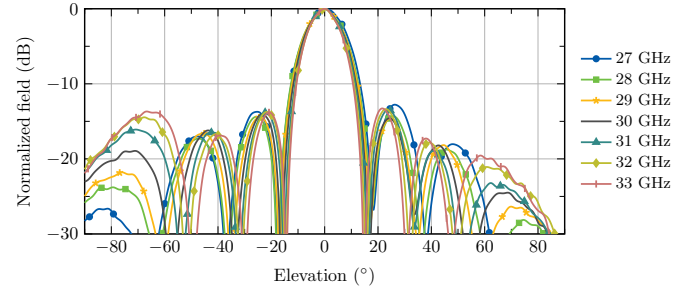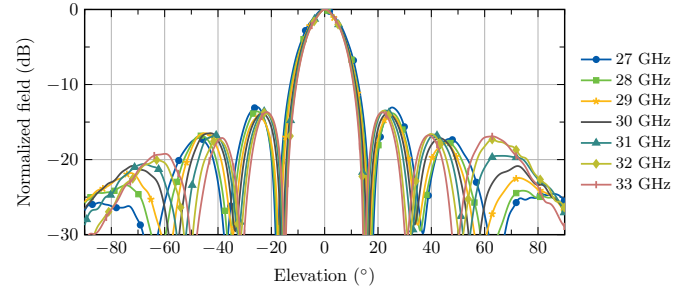

Fig. 16. Measured and simulated boresight axial ratio versus frequency.

(a)

(b)

Fig. 17. Measured copolar radiation patterns at equispaced frequencies: (a) $\phi = 0°$, and (b) $\phi = 90°$.

The measured reflection coefficient at the WR-28 port is plotted in Fig. 15, and compared to simulations. A wideband response, very close to what is predicted by simulation, is achieved without any appreciable frequency shift. Moreover, the antenna is very well matched within the band of interest, being the S_{11}-parameter below -17 dB from 27.2 GHz to 32.7 GHz. Taking the usual -10 dB threshold, the impedance bandwidth ranges from 26.9 GHz to 33.1 GHz.

The radiation characteristics of the fabricated antenna have been fully measured in an anechoic chamber by applying near-to-far field transformation. Because of its relevance, the first result reported is the boresight axial ratio, plotted in Fig. 16. The excellent prediction given by the simulation, which results in a highly-pure wideband circular polarization, should be emphasized again. Specifically, the AR parameter remains below 1 dB from 26.8 GHz to 33.3 GHz. Consequently, the measured curves so far reveal an overlapped relative bandwidth of 21%, with S_{11} and AR values better than -17 dB and 0.8 dB respectively over most of the band.

Normalized radiation patterns, sampled each 1 GHz within the array bandwidth, are represented in Fig. 17 along both main planes. Despite the wide bandwidth, the measured patterns evidence uniform array excitation over the whole band, thanks to the corporate feeding adopted. The sidelobe level keeps very stable around -13.5 dB, with a well-shaped main lobe and decaying far sidelobes except for

directions close to $-x$ axis. These asymmetric radiation patterns can be attributed to the apparent asymmetry of the H-shaped element, and logically, it is more noticeable at higher frequencies, although such far radiation never exceeds the first sidelobe level.

Lastly, the maximum directivity has been evaluated by integrating the measured pattern over the whole sampling sphere, while the antenna gain has been computed by comparison with a standard horn for both polarizations. The measured values have been plotted in Fig. 18. As expected, the maximum directivity increases with frequency, with figures mostly above 22 dBi, and a peak value of 22.4 dBi. The maximum gain reaches a sampled peak of 22.2 dBi at 33.3 GHz. Computed from these curves, the measured radiation efficiency keeps well above 85% in the whole band, with a peak value of 97%.

V. DISCUSSION

Experimental results confirm the suitability of the proposed radiating element to design wideband high-efficiency CP mm-wave array antennas with high polarization purity. Compared to previous all-metal mm-wave CP arrays, summarized in Table III, the proposed approach stands out for its low AR values sustained over a wide

TABLE III
COMPARISON OF ALL-METAL MM-WAVE CP ARRAYS

Ref.	Feeding network	Radiating element	Frequency	Number of pieces	Number of elements	Array spacing	Impedance bandwidth	3-dB AR bandwidth	1-dB AR bandwidth	Peak efficiency
[8]	Corporate R-GGW	Chamfered	30 GHz	2	4×4	$1.0\lambda_0 \times 1.0\lambda_0$	5%	>5%	2%	99%
[6]	Corporate GGW	Chamfered	60 GHz	2	16×16	$0.9\lambda_0 \times 0.8\lambda_0$	11%	8%	**	83%
[14]	Corporate RW	Chamfered	60 GHz	3*	32×32	$0.9\lambda_0 \times 0.9\lambda_0$	16%	15%	**	82%
[9]	Corporate SR RGW	Chamfered	30 GHz	3	8×8	$0.8\lambda_0 \times 0.8\lambda_0$	22%	22%	11%	85%
[11]	Corporate RGW	Septum	93 GHz	3	8×8	$1.5\lambda_0 \times 1.0\lambda_0$	31%	33%	**	85%
[12]	Series GGW	T-shaped	30 GHz	2	1×10	$0.7\lambda_0$	4%	8%	3%	98%
This work	Corporate GGW	H-shaped	30 GHz	3	4×4	$0.9\lambda_0 \times 0.9\lambda_0$	21%	>27%	22%	97%

* Antenna fabricated by diffusion bonding (three layers can be identified but fabricated in one piece).
** Not available: AR remains above the 1-dB threshold, or the bandwidth cannot be derived from the reported results.
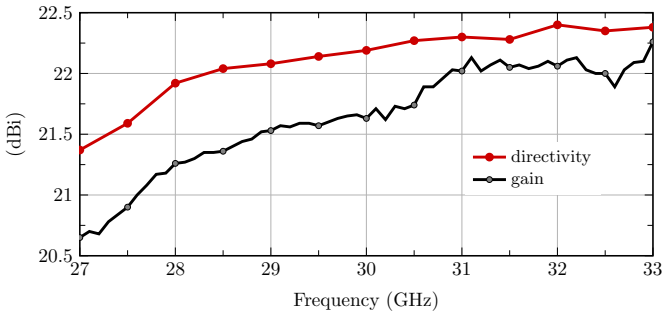

Fig. 18. Measured maximum directivity and gain versus frequency.

bandwidth. Note that it is not easy to make a fair comparison in this matter since antenna design traditionally considers the 3-dB AR threshold. In any case, this upgraded element multiplies by seven the 1-dB AR bandwidth attained by the former T-shaped element [12].

Although the successful implementation of SR techniques [9] reports similar 3-dB AR bandwidths, a higher polarization purity, with AR values below 1 dB, is only preserved in the lower part of the band. Moreover, compared to such intricate corporate SR networks, our approach proposes a much simpler array architecture, easily scalable to larger sizes and suitable for tapered illuminations. Although it is not possible to derive the 1-dB AR bandwidth from the reported results, the septum element in [11] achieves a far wider 3-dB AR band. However, the larger size of this element leads to appreciable grating lobes, which may discourage its use in some applications.

One of the main strengths of this proposal relies on the simplicity of the conceived H-shaped radiator and the corporate-feed network. This feature enables an accurate all-metal CNC fabrication at the mm-wave band, yielding an excellent agreement between simulation and measurement results. As a result, the constructed array reports a bandwidth of 21% with AR values lower than 1 dB, high return-loss, and high radiation efficiency, being a promising candidate for mm-wave applications with exigent polarization purity requirements.

REFERENCES

[1] Y.-H. Yang, S.-G. Zhou, B.-H. Sun, and X.-Z. Gao, "Design of wideband circularly polarized antenna array excited by substrate integrated coaxial line for millimeter-wave applications," *IEEE Trans. Antennas Propag.*, vol. 69, no. 12, pp. 8943–8948, 2021.

[2] L. Xiang, F. Wu, C. Yu, Z. H. Jiang, Y. Yao, and W. Hong, "A wideband circularly polarized magneto-electric dipole antenna array for millimeter-wave applications," *IEEE Trans. Antennas Propag.*, vol. 70, no. 5, pp. 3876–3881, 2022.

[3] Z. Chen, J. Tian, J.-Y. Deng, H. Liu, Z. Ma, J. Yu, and X. Chen, "Low-profile circularly polarized staircase curl antenna array with 2:1 impedance and 50% ar bandwidths for 5g mmw communications," *IEEE Trans. Antennas Propag.*, vol. 70, no. 4, pp. 3082–3087, 2022.

[4] M. Ferrando-Rocher, J. I. Herranz-Herruzo, A. Valero-Nogueira, and V. M. Rodrigo, "Circularly polarized slotted waveguide array with improved axial ratio performance," *IEEE Trans. Antennas Propag.*, vol. 64, no. 9, pp. 4144–4148, 2016.

[5] J. Cao, H. Wang, S. Mou, P. Soothar, and J. Zhou, "An air cavity-fed circularly polarized magneto-electric dipole antenna array with gap waveguide technology for mm-wave applications," *IEEE Trans. Antennas Propag.*, vol. 67, no. 9, pp. 6211–6216, 2019.

[6] M. Ferrando-Rocher, A. Valero-Nogueira, J. I. Herranz-Herruzo, and J. Teniente, "60 ghz single-layer slot-array antenna fed by groove gap waveguide," *IEEE Antennas Wireless Propag. Lett.*, vol. 18, no. 5, pp. 846–850, 2019.

[7] M. Zhang, T. Yamamoto, J. Hirokawa, and M. Ando, "A wideband circularly polarized corporate-fed waveguide aperture array in the 60 ghz band," *IEEE Antennas Wireless Propag. Lett.*, vol. 20, no. 9, pp. 1824–1828, 2021.

[8] M. Ferrando-Rocher, J. I. Herranz-Herruzo, A. Valero-Nogueira, and A. Vila-Jiménez, "Single-layer circularly-polarized ka-band antenna using gap waveguide technology," *IEEE Trans. Antennas Propag.*, vol. 66, no. 8, pp. 3837–3845, 2018.

[9] M. Akbari, A. Farahbakhsh, and A. Sebak, "Ridge gap waveguide multilevel sequential feeding network for high-gain circularly polarized array antenna," *IEEE Trans. Antennas Propag.*, vol. 67, no. 1, pp. 251–259, 2019.

[10] M. Ferrando-Rocher, J. I. Herranz-Herruzo, A. Valero-Nogueira, and B. Bernardo-Clemente, "Single-layer sequential rotation network in gap waveguide for a wideband low-profile circularly polarized array antenna," *IEEE Access*, vol. 10, pp. 62 157–62 163, 2022.

[11] K. Wu, Y. Yao, X. Cheng, T. Xiu, J. Yu, and X. Chen, "Wideband circularly polarized septum antenna array with ridge gap waveguide feeding network for wireless application," *IEEE Trans. Antennas Propag.*, vol. 70, no. 5, pp. 3882–3887, 2022.

[12] J. I. Herranz-Herruzo, M. Ferrando-Rocher, A. Valero-Nogueira, and B. Bernardo-Clemente, "Novel asymmetric t-shaped radiating element for circularly-polarized waveguide slot arrays," *IEEE Trans. Antennas Propag.*, vol. 69, no. 11, pp. 7452–7461, 2021.

[13] J. I. Herranz-Herruzo, M. Ferrando-Rocher, and A. Valero-Nogueira, "Multimode coupled slots for wideband circularly-polarized mm-wave all-metal antennas," in *2022 IEEE International Symposium on Antennas and Propagation and USNC-URSI Radio Science Meeting (AP-S/URSI)*, 2022, pp. 399–400.

[14] Y. Miura, J. Hirokawa, M. Ando, Y. Shibuya, and G. Yoshida, "Double-layer full-corporate-feed hollow-waveguide slot array antenna in the 60-ghz band," *IEEE Trans. Antennas Propag.*, vol. 59, no. 8, pp. 2844–2851, 2011.

[15] P. Kildal, E. Alfonso, A. Valero-Nogueira, and E. Rajo-Iglesias, "Local metamaterial-based waveguides in gaps between parallel metal plates," *IEEE Antennas Wireless Propag. Lett.*, vol. 8, pp. 84–87, 2009.

[16] A. Vosoogh, P.-S. Kildal, and V. Vassilev, "Wideband and high-gain corporate-fed gap waveguide slot array antenna with etsi class ii radiation pattern in v-band," *IEEE Trans. Antennas Propag.*, vol. 65, no. 4, pp. 1823–1831, 2017.